Diffusion of cytokines in live lymph node tissue using microfluidic integrated optical imaging

A.E. Ross[a, 1] and R.R. Pompano[a,*]

Accepted Manuscript

Analytica Chimica Acta (2018) 1000, 205-213

https://doi.org/10.1016/j.aca.2017.11.048

[a] Department of Chemistry
University of Virginia
McCormick Rd.
PO Box 400319
Charlottesville, VA USA 22904

* Corresponding author
Email: rrp2z@virginia.edu
Phone: 1-434-982-1825

1. Present Address: Department of Chemistry, University of Cincinnati, 301 Clifton Court. Cincinnati, OH USA 45220

Abstract:

Communication and drug efficacy in the immune system rely heavily on diffusion of proteins such as cytokines through the tissue matrix. Available methods to analyze diffusion in tissue require microinjection or saturating the tissue in protein, which may alter local transport properties due to damage or rapid cellular responses. Here, we developed a novel, user-friendly method – Microfluidic Integrated Optical Imaging (micro-IOI) – to quantify the effective diffusion coefficient of bioactive proteins in live tissue samples ex vivo. A microfluidic platform was used to deliver picograms of fluorescently labelled cytokines to microscale regions within slices of murine lymph node, and diffusion was monitored by widefield fluorescence microscopy. Micro-IOI was validated against theory and existing methods. Free diffusion coefficients were within 8 % and 24 % of Stokes-Einstein predictions for dextrans and cytokines, respectively. Furthermore, diffusion coefficients for dextrans and proteins in a model matrix were within 1.5-fold of reported results from fluorescence recovery after photobleaching (FRAP). We used micro-IOI to quantify the effective diffusion of three cytokines from different structural classes and two different expression systems – tumor necrosis factor alpha (TNF-α), interferon gamma (IFN-γ), and interleukin-2 (IL-2), from human and mouse – through live lymph node tissue. This is the first method to directly measure cytokine transport in live tissue slices, and in the future, it should promote a deeper understanding of the dynamics of cell-cell communication and enable targeted immunotherapy design.

Keywords: local delivery, inflammation, tumor necrosis factor alpha, interleukin-2, interferon gamma

1. Introduction:

Diffusion of secreted proteins through the extracellular space is fundamental to cell-cell communication and organized tissue-level responses. Diffusion, coupled with binding events and interstitial fluid flow, establishes concentration gradients that are essential to tissue morphogenesis, directional cell growth, chemotaxis within and between tissues, and drug delivery (1–7). In tissue, unlike in a simple buffer solution, diffusion is hindered by the geometry of the extracellular space, by binding to cell-surface receptors or the extracellular matrix (ECM), and by non-specific charge-charge interactions (8, 9). The degree of hindrance, or tortuosity, for a given analyte is quantified by comparing the "effective diffusion" in tissue to the "free diffusion" in buffer (10). Tortuosity in brain varies based on the health and region of the tissue (11–13), and for bioactive molecules, may vary also with the presence of binding sites in the ECM and on cell surfaces (9). Quantifying effective diffusion and tortuosity in organs such as the brain has provided critical insights into the mechanisms of drug delivery and inflammatory diseases (10, 14). Unfortunately, localized diffusion data for bioactive proteins in smaller organs remains difficult to obtain. This paper describes a new analytical method to quantify diffusion of bioactive proteins in live tissue, specifically in lymph node slices, and provides the first diffusion coefficients for cytokines in healthy lymph node tissue.

Several techniques are available to analyze diffusion of macromolecules through biological tissues (10, 15–17), but these may not be optimal for use with bioactive molecules in sensitive tissue samples. The gold-standard method is pressure ejection of fluorescently-labelled proteins coupled to integrated optical imaging, as pioneered by Nicholson (8, 10, 18). Pressure ejection approximates a point source by delivering a small volume of analyte to the tissue through a micropipette as small as 1 - 2 μm at the tip (19, 20). Timelapse images are collected and analyzed by linescan to quantify the spread of the protein over time. This approach has been used productively for 25 years, predominately in brain, to quantify diffusion of fluorescently

labelled probes and thus elucidate the geometric properties of the extracellular space. However, probe insertion causes mechanical damage to the tissue that generates rapid reactivity (21, 22). Diffusion distances for metabolites and proteins through tissue are on the order of 50 - 200 μm (6), therefore, danger signals could potentially extend within minutes of probe insertion over a region ~ 100 – 400 μm in diameter, the same length scale as substructures within the lymph node and other organs. Local damage surrounding the probe may be particularly detrimental to reactive organs such as the lymph node, whose rapid response to tissue damage (23) may alter the local microenvironment. An alternative method is fluorescence recovery after photobleaching (FRAP), in which the sample is saturated with a fluorescently-labelled protein and locally photobleached. Timelapse images are collected to quantify diffusion of the remaining protein into the bleached area over time (16). FRAP has been used to quantify diffusion of protein-sized analytes in both gels (24, 25) and tissue (26–28), using inert dextrans and proteins such as albumin. However, soaking lymph node tissue in bioactive cytokines may induce a rapid cellular response that could alter transport properties.

Methods are needed to analyze protein diffusion in the lymph node in order to inform the development of targeted immunotherapies and reveal mechanisms of cell-cell communication in adaptive immunity. The lymph node is highly structured, much like the brain, and its organized structure is critical for proper initiation of adaptive immunity (29–32). Cell-cell communication in the lymph node is transmitted largely through secreted proteins called cytokines (33, 34), which serve as drug targets because their local concentrations guide inflammatory and immune events (35–38). Cytokines act both locally and across the node, indicative of a diffusing signal (39–41). Many cytokines bind the extracellular matrix, which may contribute to gradient formation (42, 43), and convection by interstitial flow likely also affects their distribution (44). Despite intense interest in building predictive models of cytokine signaling for mechanistic studies and immunotherapy

design (45–47), the diffusion coefficient of cytokines through lymph node tissue remains unmeasured.

In this paper, we describe a new method to quantify diffusion of bioactive proteins in live lymph node tissue. In order to limit local tissue damage and reactivity, we utilized microfluidic delivery of the protein in combination with IOI (Micro-IOI). A microfluidic channel terminating in a port was used to deliver bioactive cytokines to discrete regions of lymph node tissue. IOI image-analysis methods were developed to accommodate the background of the microfluidic channel, and the resulting Micro-IOI method was validated against FRAP in slices of agarose gel and validated for free diffusion of both dextrans and proteins. Next, the method was used to quantify the diffusion in tissue of three murine cytokines: IL-2, TNF-α, and IFN-γ, which play critical roles in the immune response and differ in molecular weight, oligomerization, and structure. We sought to isolate the effect of glycosylation on diffusion by testing cytokines expressed in mammalian cells versus in E. coli and finally calculated the tortuosity experienced by these proteins through the tissue. .

2. Materials and Methods:

2.1 Preparation of fluorescently-labelled probes:

Fluorescein-labelled dextran, anionic (FITC-dextran) in varying molecular weights and Alexa Fluor 647-labelled 10-kDa dextran were obtained from Life Technologies and stored at -20 °C in 1x phosphate buffered saline (PBS: 137 mM Sodium chloride, 10 mM sodium phosphate dibasic, 2.7 mM potassium chloride, and 1.8 mM potassium phosphate monobasic). Recombinant murine TNF-α, IFN-γ, and IL-2, expressed in E.coli, were obtained from Peprotech, and recombinant human TNF-α, IFN-γ, and IL-2, expressed in HEK 293 cells, were obtained from Acro Biosystems. Cytokines were covalently conjugated to a fluorophore by incubating with excess Alexa Fluor 647 NHS-ester (Life Technologies) for 1 hr at room temperature, followed by 2 hours at 4 °C. Excess

dye was removed by repeated centrifugation through an EMD Millipore Amicon Ultra-2 centrifugation unit (Fisher Scientific) with a 3-kDa molecular weight cut-off. The degree of labelling was determined using a Nanodrop 1000 (Thermo Scientific), and was 3, 6, and 2 mol dye/mol protein for mouse IL-2, TNF-α, and IFN-γ, respectively. The degree of labelling for human IL-2, TNF-α, and IFN-γ, was 1.4, 2, and 2.6, respectively. Labelled cytokines were stored at -20 °C in 1x PBS.

2.2 Microfluidic device fabrication:

The three-layer device was fabricated according to published procedures (48). Briefly, the top and bottom layers (tissue culture chamber and microfluidic channels) were fabricated using standard soft lithography. Transparency masks were drawn in AutoCAD LT 2015 and printed at 20,000 DPI (CAD/Art Services Inc, Bandon OR). Master molds were fabricated using SU-8 3050 photoresist (Microchem, Westborough MA, USA) on 3" silicon wafers in a class 1000 cleanroom. Polydimethylsiloxane (PDMS) was used at a 10:1 ratio of silicon elastomer base to curing agent (Ellsworth Adhesives, Germantown WI, USA) to create replicas of the device. Inlet and outlet holes were punched into the top layer prior to bonding using a 0.75 mm I.D. tissue punch (World Precision Instruments, Sarasota FL, USA) to accommodate nonshrinkable PTFE TT-30 tubing with 0.012" I.D. and 0.009" wall thickness (Weico Wire, Edgewood NY, USA for delivery. The tissue culture chamber (top layer) was punched using a 12 mm tissue punch. The middle layer (exit port) consisted of a 250-µm thick PDMS sheet (Stockwell Elastomerics, Inc, PA USA) that was laser etched (Versa Laser 3.5, Universal Laser Systems, Scottsdale AZ, USA) to create a 80-µm exit port for the microfluidic channel. All three layers were manually aligned and permanently bonded with air plasma (Tegal Plasmod).

2.3 Free diffusion experiment and Micro-IOI validation in gels:

Prior to the experiment, the microfluidic channel was filled completely with the analyte of interest and the outlet was plugged. Plugging the outlet ensured that the quantity of analyte delivered was known precisely based on the concentration and flow rate of delivery. The device was placed on the stage of a Zeiss AxioZoom macroscope (Carl Zeiss Microscopy, Germany) equipped with an Axiocam 506 Mono camera. For measurements of free diffusion, the tissue culture chamber was filled with 0.3 % w/v agarose in 1x PBS to minimize convective flow (18). Temperature was maintained at 37 °C by using a stage-top mini-incubator with heated base and heated lid, equipped with a temperature probe (Bioscience Tools, San Diego, CA). Analyte solutions were loaded into a 50 µL Hamilton Model 1710 RN syringe with 26s gauge large hub needle, and delivered through the microchannel by using a Chemyx syringe pump (Houston TX, USA). FITC-dextran (0.05 mg/mL in 1x PBS) was delivered for 5 s at 0.4 µL/min. Time-lapse images (14 bit, using Zeiss filter set #38 for fluorescein) were collected at 1-s intervals for a few seconds prior to delivery and for the duration of delivery. Immediately after delivery, the pump was stopped to halt convection, and time-lapse images were recorded every 30 s for 180 s to watch the spread of the fluorescent signal. Free diffusion of each Alexa Fluor647-labelled cytokine (0.01 mg/mL) was measured similarly, using the Cy5 (#50) filter set.

To validate micro-IOI measurements in gels, 300-µm thick slices of low-melting point agarose (2, 4, 6, or 8 % w/v; Lonza, Walkersville MD, USA) were prepared using a Leica VT1000S (Bannockburn, IL, USA) vibratome. The microfluidic channel was filled and plugged as described above, and an agarose slice was submerged in 1x PBS in the tissue culture chamber. A stainless steel washer (10 mm O.D. and 5.3 mm I.D., Grainger USA) was placed on top of the slice to anchor it down. The analyte solution (0.05 mg/mL 3-kDa FITC-dextran, 10-kDa FITC-dextran, or fluorescein-conjugated ovalbumin (FITC-OVA, Life Technologies) was delivered to the agarose slice for 5 s. Temperature control and imaging were performed as for free diffusion.

2.4 Lymph node slice harvest and staining:

Lymph node slices were prepared as previously reported.(48) All animal work was approved by the Animal Care and Use Committee at the University of Virginia. Female C57BL/6 mice between 6-12 weeks of age (Jackson Laboratory, USA) were housed in a vivarium and given food and water *ab libitum*. On the day of the experiment, mice were anesthetized with isoflurane and euthanized by cervical dislocation. Six peripheral lymph nodes (inguinal, brachial, and axillary) were removed and placed in ice-cold DPBS without calcium or magnesium (Lonza, Walkersville MD, USA, #17-512F) with 2 % v/v heat-inactivated fetal bovine serum (FBS, Gibco, Fisher Scientific, 100 % US Origin, 1500-500 Lot 106B14). Lymph nodes were embedded in 6 % w/v low melting point agarose prepared in 1x PBS, which was placed on ice to harden. A 10-mm tissue punch (World Precision Instruments) was used to collect a block of agarose containing the lymph node. The block was glued onto a mounting stage and sliced to 300-µm thick using a Leica VT1000S (Bannockburn, IL, USA) vibratome set to a speed of 90 and frequency of 3. Slices were collected using a paint brush and placed in a "complete RPMI": RPMI (Lonza 16-167F) supplemented with 10 % FBS, 1x L-glutamine (Gibco Life Technologies, 25030-081), 50 U/mL Pen/Strep (Gibco), 50 µM beta-mercaptoethanol (Gibco, 21985-023), 1 mM sodium pyruvate (Hyclone, GE USA), 1x non-essential amino acids (Hyclone, SH30598.01), and 20 mM HEPES (VWR, 97064-362). Slices were kept in a sterile incubator at 37 °C with 5 % CO_2 for one hour prior to use. Slices of agarose without tissue were prepared similarly for the Micro-IOI validation experiments.

Prior to the experiment, the tissue slices were immunostained to show structure. Slices were blocked with 20 µL of 25 µg/mL LEAF purified anti-mouse CD16/32 antibody (Clone 93, Biolegend, San Diego CA, USA) for 10 min, then stained with anti-mouse CD45R/B220 antibody (10 µL of fluorophore-antibody conjugate added to the 20 µL of block solution) for 60 minutes in the cell culture incubator. In experiments using Alexa Fluor 647-labelled diffusion probes, slices

were labelled using 6.7 µg/mL FITC-anti-mouse B220 (clone RA3-6B2, Biolegend), which was imaged using Zeiss filter set #38 for fluorescein. In experiments using FITC-labelled diffusion probes, slices were labelled using 13 µg/mL Rhodamine-labelled anti-mouse B220 (Biolegend), which was imaged using filter set #43. After staining, slices were washed three times with 1x PBS and stored in complete RPMI in the incubator until use. In preliminary work, we found that this procedure labeled B220-positive B cells selectively, with a low level of Fc-mediated off-target binding occurring in the sinus and cortical region of the tissue.

2.5 Experimental measurement of diffusion in live lymph node slices:

For delivery to tissue, the channel was filled with the analyte of interest (fluorescently labelled dextran or cytokine) and the outlet was plugged. A live, immunostained lymph node slice was placed inside the PBS-filled tissue culture chamber, and a washer was placed on top. The tissue was aligned manually to place a region of interest over the delivery port. The analyte was delivered for 3 - 5 s to the T-cell or B-cell/Cortex region of the slice, and imaging was performed at 37 °C as described above. In most tissue experiments, Alexa Fluor 647-labelled probes were used in order avoid tissue autofluorescence in the green channel. In one experiment, to test the extent to which the fluorophore affected diffusion, FITC 10-kDa dextran was used instead.

2.6 Image analysis to determine experimental diffusion coefficients:

Micro-IOI image analysis was based on the method developed by Nicholson (see Supplemental Figure 1 for flow chart) (18, 49). Images were analyzed using Zen Lite software 2.3 (Zeiss) and Image J 1.50i. For each experiment, a linescan was collected from a background fluorescence image taken before delivery, and this linescan was subtracted from all later time points.(18) This background subtraction removed autofluorescence of the tissue and dim scattered fluorescence from the microchannel below the sample. Images for analysis were collected at 30, 60, 90, 120, 150, and 180 s after delivery. The first 30 s after delivery were excluded due to possible residual

convection from the microfluidic port. When working in tissue, the linescan was drawn so that it did not extend past the borders of the tissue. In all cases, the linescan was across the channel rather along it, to minimize its contribution to the background fluorescence.

During measurements made in optically clear samples (i.e. for free diffusion and agarose gel), an intense fluorescent signal was observed in the center of the linescan due to the fluorescent solution in the port. This artifact was manually excluded prior to analysis by selecting the x-coordinates that pertained to the port and a small section surrounding the port (SI Figure 2). The excluded region was constant for all time points for a given experiment.

Diffusion of the analyte after microfluidic delivery was approximated as 2-dimensional point-source diffusion. With these flow rates and microfluidic port diameter, the initial distribution was several hundred microns across (48); thus, the behavior was that of a "virtual" instantaneous point source at an earlier time (18, 20). We assumed that over the timescale of measurement (up to 180 s), consumption or depletion of the analyte was negligible. The concentration distribution *C* [mol/μm^3] arising from 2-dimensional point-source diffusion through a thick slice is described by the following equation,

$$C(r,t) = \frac{N}{4\pi DtL} e^{-r^2/4Dt}, \quad (1)$$

where *N* is the number of moles of analyte released [mol], *D* is the diffusion coefficient [μm^2/s], *t* is the time since release from the virtual point source [s], *L* is the vertical thickness of the slice [μm], and *r* is the radial position from the source [μm].

To obtain the diffusion coefficient for each sample, intensity data from each linescan were fit with a Gaussian Equation (Eq. 2) in Graphpad Prism 7.

$$y = Ae^{-0.5(x/\sigma)^2} \quad (2)$$

where A is the amplitude of the curve, *x* is the distance along the linescan (μm), and σ is the standard deviation of the Gaussian curve. Comparison of Eq. 1 and 2 yields the following relationship:

$$\sigma^2 = 2Dt \quad (3)$$

Therefore, the diffusion coefficient for each trial was estimated by determining the slope of a linear regression of $\sigma^2/2$ vs *t*.

2.7 Prediction of free diffusion coefficients:

Free diffusion coefficients were estimated based on the Stokes radii of the molecules. Stokes radii for dextrans were obtained from the vendor. For cytokines, the Stokes radius (*R*) was estimated based on molecular weight, by assuming the protein was a spherical structure composed of closely packed atoms. This assumption yields Eq. 4 (50).

$$R = \left(\frac{3V}{4\pi}\right)^{\frac{1}{3}} = \left(\frac{3}{4\pi}\frac{MW}{N_A}v\right)^{\frac{1}{3}} \quad (4)$$

Here, V is defined as the volume of a single protein molecule [cm^3], *MW* is the molecular weight of the protein [g/mol], N_A is Avogadro's number (6.02 x 10^{23} molecules/mol), and *v* is the partial specific volume [cm^3/g], i.e. the inverse of the density. Protein density is estimated to be 1.37 cm^3/g, so the partial specific volume is 0.73 g/cm^3 (50). The assumption of closely packed atoms will underestimate the radius of proteins that have a loose tertiary structure; such proteins would likely diffuse in free solution more slowly than predicted by this estimate.

The free diffusion coefficient was estimated using the Stokes-Einstein equation (Eq. 5), where *k* is the Boltzmann constant (1.38 x 10^{-16} g•cm^2/ s^2•K), *T* is temperature [K], η is the solvent viscosity (0.0069 g/cm•s for PBS at 37°C), and *R* is the Stokes radius [cm].

$$D = \frac{kT}{6\pi\eta R} \quad (5)$$

2.8 Tortuosity:

Tortuosity (λ) describes the degree of hindrance experienced by the molecule within the matrix compared to diffusion in free solution (10). The equation for tortuosity was expressed in terms of the free diffusion (*D*) and effective diffusion coefficient (D^*) within the tissue (Eq. 6):

$$\lambda = \sqrt{\frac{D}{D^*}} \tag{6}$$

Standard errors, *SEM*, for tortuosity were calculated by propagation of the experimental standard error of *D* and *D** (Eq. 7), assuming independent errors:

$$SEM_\lambda = \frac{\lambda}{2}\sqrt{\left(\frac{SEM_D}{D}\right)^2 + \left(\frac{SEM_{D^*}}{D^*}\right)^2} \tag{7}$$

2.9 Statistics:

All values were expressed as mean ± SEM unless otherwise indicated. GraphPad Prism 7 was used to compute all statistics (GraphPad Software Inc., La Jolla, CA USA). Differences were considered significant at $p < 0.05$.

3. Results and Discussion:

3.1 Microfluidic integrated optical imaging (Micro-IOI) for diffusional analysis of bioactive proteins:

To analyze diffusion in the highly structured environment of the lymph node (Fig. 1a), we developed a microfluidic delivery method coupled to integrated optical imaging that limits tissue damage in the region of interest, is compatible with bioactive molecules, and is easily applied to any biological tissue. We took advantage of a microfluidic device recently developed by our laboratory for spatially resolved delivery of proteins to live lymph node slices (48), simplifying the design for this study to a single channel and delivery port. The device consisted of three stacked

PDMS layers: a single 100-µm x 100-µm microchannel (bottom), a thin layer of PDMS with a single exit port (80-µm diameter) aligned over the channel, and a tissue chamber (top) (Fig. 1b-d). The chamber allows complete submersion of the tissue sample for enhanced viability, and the use of a microchannel provides non-invasive, controlled delivery of precise volumes to sub-regions of the tissue (48, 51–53). We have previously shown that lymph node slices retain viability for at least 6 hours after slicing and at least 4 hours on the microfluidic chip (48); all diffusion experiments were performed within this timeframe.

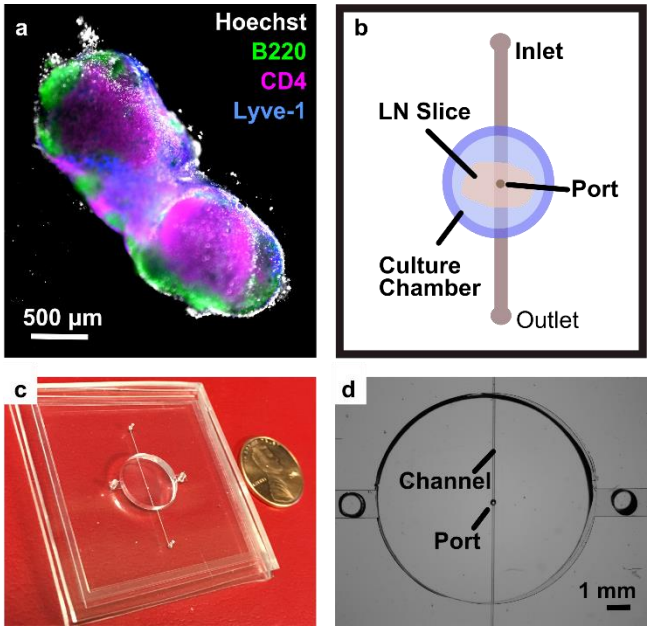

Figure 1: Design and prototype of device for microfluidic integrated optical imaging (Micro-IOI) to analyze diffusion in live lymph node tissue. a) Live lymph node slices had substructures that were visible after live immunostaining, here with Rhodamine-anti-B220 for B cells (green), FITC-anti-CD4 $(Fab)_2$ for T cells (pink), eFluor 660-anti-Lyve-1 for lymphatics (blue), and Hoechst nuclear counterstain (gray). b) Top-view schematic of microfluidic device. c) Photograph of assembled device and d) micrograph image of culture chamber, with the underlying channel and port visible.

To analyze diffusion, the fluorescently labelled analyte was delivered to the sample in a brief pulse (3 – 5 sec), after which the pump was stopped and the lateral spread was monitored

every 30 s using widefield fluorescence microscopy (Fig. 2a-b). Data was analyzed by established IOI techniques (18): a linescan from each time point was fit with a Gaussian distribution to obtain the standard deviation (σ) of the distribution, and the diffusion coefficient was obtained from a linear regression of $\sigma^2/2$ versus time (see Methods and SI Figure 1). The linescans were background subtracted by using an image collected prior to delivery, to account for dim fluorescence from the microchannel below the tissue. Furthermore, for optically clear samples, a small central portion of the linescan was excluded to eliminate false signal arising from the port beneath the tissue (SI Figure 2). The latter step was not required in tissue, which was opaque enough to obscure the light from the port.

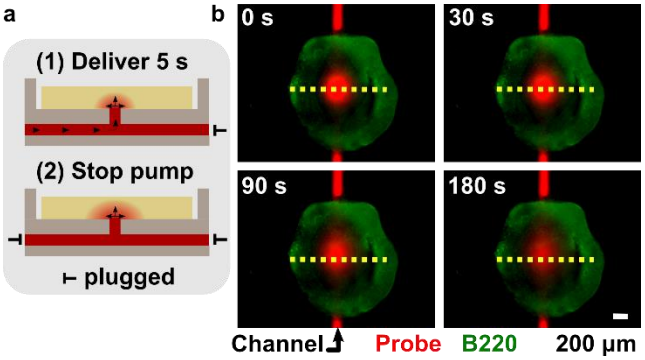

Figure 2: Experimental assay for diffusional analysis in tissue. a) Side-view schematic representing the two-step experimental procedure. b) Selected time lapse images showing a live lymph node slice, immunostained with FITC-anti-mouse B220 (green), on the microfluidic chip during an experiment. A fluorescent protein (red; images show TNF-α) was delivered through the channel into the tissue, and the end of delivery designated as 0 s. Images collected at 30, 90, and 180 s after delivery are shown. Yellow dotted line represents linescan along which diffusion was quantified. Timelapse movies of delivery and diffusion are provided in the Supplement (Movies S1 and S2, respectively).

3.2 Micro-IOI validation:

Micro-IOI was validated for diffusion of protein-sized analytes in both free solution and agarose gel. Dextrans are branched polysaccharides, similar in size to proteins, and are often used to model diffusion of non-binding analytes in tissue and gels (18, 24, 54). We quantified the free diffusion of FITC-labelled 10- and 40-kDa dextran and five Alexa Fluor 647-labelled cytokines

(Table 1). The results were compared to the predictions of the Stokes-Einstein equation. The free diffusion coefficients for 10- and 40-kDa dextran were within 8 % and 1 % of the prediction, respectively; free diffusion coefficients of all cytokines were within 24 % of the prediction. Variation between trials for free diffusion measurements was similar to that reported using traditional IOI (55).

Table 1: Diffusion of dextran and cytokines in 2 % agarose and lymph node tissue at 37 °C. All values of D are x 10^{-7} cm^2/s and mean ± SEM. Number of independent samples (n) shown in parenthesis.

Analyte	Molecular Weight (kDa)	Stokes Radius (nm)	Calculated D_{free}†	Measured D_{free}‡	2% Agarose D_G	Micro-IOI T-cell zone D_{eff}	Micro-IOI B-cell/Cortex D_{eff}
Dextran	10	2.30	14	13 ± 4 (7)	8.9 ± 1.9 (5)	6.7 ± 2 (4)	6.8 ± 3 (6)
Dextran	40	4.50	7.3	7.4 ± 3 (4)	4.7 ± 1.4 (5)	-	-
Murine IL-2 (E.coli)	17.2	1.71*	19	25 ± 6 (4)	14 ± 2.8 (4)	10.5 ± 2.0 (7)	6.5 ± 2.0 (5)
Human IL-2 (HEK 293)	17	1.71*	19	23 ± 4.2 (5)	18 ± 3 (4)	9.2 ± 2 (4)	6.3 ± 2.5 (5)
Murine IFN-γ (E.coli)	15.6	1.65*	20	17 ± 4 (5)	15 ± 4.0 (4)	10.6 ± 1.7 (7)	7.5 ± 2.0 (8)
Murine TNF-α (E.coli)	17.3 (monomer)	1.71*	19	19 ± 0.9 (4)	17 ± 3.0 (4)	4.4 ± 1.3 (8)	5.4 ± 1.2 (5)
Human TNF-α (HEK 293)	54 (trimer)	2.50*	13	15 ± 3 (4)	13 ± 1.5 (5)	11 ± 3 (5)	6.9 ± 1.0 (7)

* Estimated from the molecular weight reported from the vendor (Peprotech for E.coli and Acro Biosystems for HEK 293), using Eq. 4.
† Calculated from Stokes-Einstein equation (Eq. 5) at 37 °C.
‡ Measured in 0.3 % agarose in 1x PBS.

Next, the performance of micro-IOI was tested in slabs of agarose gel as a model of tissue. Agarose hydrogel is frequently used to model the physical characteristics of brain tissue and other complex matrices (56). Linescans for both 10- and 40-kDa dextran decreased in intensity and increased in width over time, as expected for a process mediated by diffusion (Fig. 3a-b). As

expected, both probes exhibited restricted diffusion in 2 % agarose compared to in free solution, and increasing the size of the dextran or the concentration of agarose further restricted diffusion through the gel. Specifically, 40-kDa dextran experienced higher hindrance to diffusion than 10-kDa dextran in 2 % agarose (Fig. 3c and Table 1). Similarly, increasing the agarose concentration over the range 2 – 8 % w/v reduced the effective diffusion coefficient for both dextrans (Fig. 3d and Table 1; $p = 0.02$ by two-way ANOVA). This trend was comparable to previous reports showing protein diffusion in varying percentages of agarose gel using a refractive index method (57).

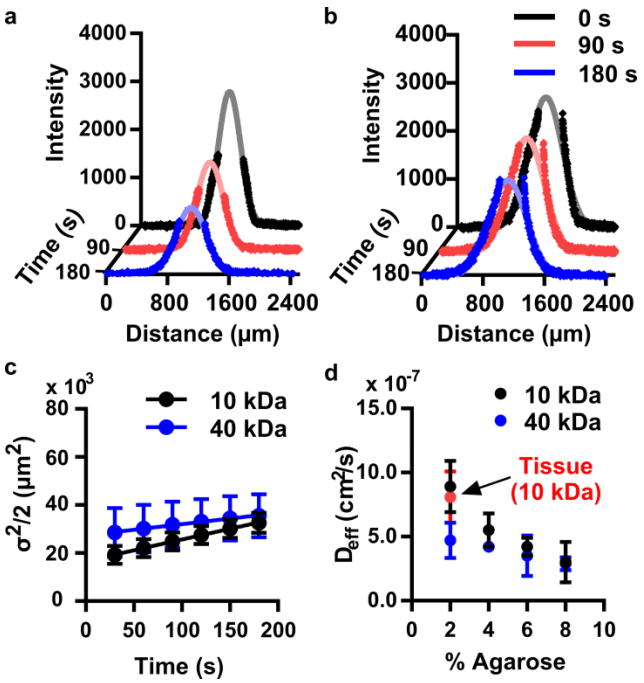

Figure 3: Micro-IOI reproduced expected trends for diffusion in of dextrans in agarose gel. Representative linescan data at 3 time points for (a) 10-kDa dextran and (b) 40-kDa dextran, shown in bold dots. A portion of the data at the peak was excluded to remove an artifact from the brightness of the port (SI Fig. 2), and the remaining data were fit with a Gaussian distribution (pale solid line) to obtain the standard deviation of the curve (σ). All Gaussian fits in agarose had $r^2 \geq 0.90$. (c) The slope of mean squared displacement versus time gives the diffusion coefficient. 10-kDa dextran had a larger diffusion coefficient than 40-kDa dextran in 2 % agarose. $r^2 = 0.99$ for both curves. Data for individual samples are provided in SI Fig. 3. (d) The diffusion coefficient decreased as a function of increasing percent agarose for both dextrans. Diffusion of 10-kDa dextran in lymph node slices (red) closely resembled the diffusion in 2 % agarose.

Finally, we directly compared the effective diffusion coefficients from micro-IOI to results obtained by Pluen et. al using FRAP (24). FITC-labelled 3-kDa dextran, 70-kDa dextran, and chicken egg ovalbumin (OVA) were delivered to 2 % agarose gel at 25 °C (Table 2, n = 4-5). Micro-IOI diffusion coefficients were within two-fold of those from FRAP, showing good agreement (Table 2). Pluen et. al tested 4.4 kDa dextran instead of the 3 kDa dextran used here, which may partially explain the 35 % difference in values for that probe.

Table 2: Diffusion measurement with Micro-IOI was comparable to FRAP in 2% agarose gel at 25 °C. All values are x 10^{-7} cm^2/s and mean ± SEM (n = 4-5).

Analyte	Molecular Weight (kDa)	Stokes Radius (nm)	Micro IOI D_G (cm^2/s)	FRAP* D_G (cm^2/s)
Dextran	3	1.4	16 ± 1.3	10.5†
Dextran	70	6.0	3.5 ± 1.0	2.9
Ovalbumin	45	3.2	4.5 ± 1.0	4.0 x10^{-7}

*A. Pluen et. al, Biophysical Journal, 1999, 542-552

† Value for 4.4 kDa Dextran

3.3 Diffusion of dextran in live lymph node tissue:

It is useful to analyze the diffusion of non-binding analytes, such as dextrans, in tissue, because they reveal physical characteristics of the extracellular space such as tortuosity (10). These characteristics are not well understood in lymph nodes (58). The lymph node can be roughly subdivided into two regions: a central T-cell zone, or deep paracortex, where T cells interact with antigen-presenting dendritic cells, and an outer region, or cortex, that contains multiple ovoid follicles of antibody-producing B cells as well as other cells. B cell follicles and surrounding cortical tissue have a different underlying stromal structure than the T cell zone (59, 60), and we tested whether diffusion coefficients differed between regions. Zones were distinguished by incubating the slices with a fluorophore-labelled antibody against B220, a B cell marker, prior to micro-IOI. The T-cell zone was defined as the absence of B220 staining in a

central region of the tissue, while the B220-bright regions were assigned to the B-cell/cortex zone. We used Micro-IOI to quantitate the effective diffusion coefficient of a non-binding analyte whose size is similar to a typical cytokine, 10-kDa dextran, in substructures within the lymph node in order to determine their geometric tortuosity.

Diffusion of Alexa Fluor 647-labelled 10-kDa dextran was analyzed in the T-cell zone (Fig. 4a,c) and the B-cell/Cortex zone (Fig. 4b,c) of live lymph node slices (Table 1). The 10-kDa dextran had the same effective diffusion coefficient in both the T-cell and B-cell/Cortex zones. As a control, we also tested fluorescein-conjugated dextran, and found that its diffusion was indistinguishable from the Alexa Fluor 647-conjugate (SI Fig. 4), confirming that the results were not due to an artifact related to the choice of fluorophore (61). This result suggests that the structure of the extracellular space is similar between the T cell zone and the cortex or B cell zone. The calculated tortuosity for 10-kDa dextran in both zones was estimated to be 1.4 in these naïve, unstimulated slices (Table 3). For reference, measurements of 10-kDa dextran diffusion in rat cerebral cortex using traditional IOI yielded a tortuosity of 1.6 (18), somewhat higher than our result for lymph node (2.6-fold vs 2.0-fold reduction in diffusion coefficient in brain and lymph node, respectively). If upheld by future experiments, we speculate that the difference may be related to differences in cytoarchitecture; for example, cells in the lymph node are primarily small and semi-spheroidal, whereas the brain features dense networks of axons. Differences in the structure of the extracellular matrix could also play a role (62).

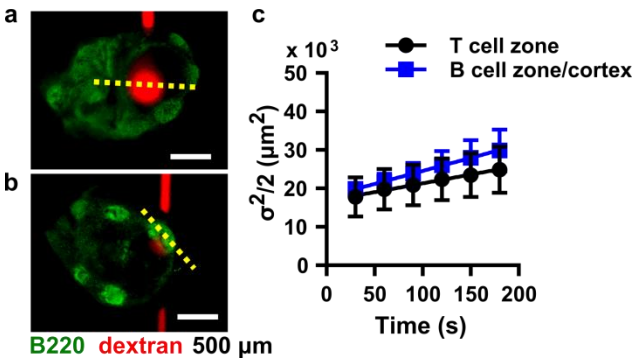

Figure 4: Diffusion of 10-kDa dextran in live lymph node slices. Lymph node slices were immunostained with FITC-anti-mouse B220 (green) to show structure. Alexa Fluor 647-labelled 10-kDa dextran (red) was delivered for 5 s to either (a) the T cell zone or (b) B cell/Cortex zone of the slice. (c) The mean squared displacement as a function of time was plotted for both zones. The slope of the curve gives the diffusion coefficient (tabulated in Table 2; SI Fig. 5 shows individual slices). Values are mean ± SEM (n = 4-6).

Table 3: Tortuosity of dextran and cytokines in 2% agarose hydrogel or healthy murine lymph node. All diffusion coefficients were obtained at 37 °C.

Analyte	**Tortuosity**		
	2% agarose	**T cell zone**	**B-cell/ Cortex zone**
10 kDa Dextran	1.2 ± 0.2	1.4 ± 0.3	1.4 ± 0.9
IL-2 (E.coli) Murine	1.3 ± 0.2	1.5 ± 0.2	2.0 ± 0.4
IL-2 (HEK 293) Human	1.1 ± 0.1	1.6 ± 0.2	1.9 ± 0.4
IFN-γ (E.coli) Murine	1.1 ± 0.2	1.3 ± 0.2	1.5 ± 0.3
TNF-α (E.coli) Murine	1.1 ± 0.1	2.1 ± 0.3	1.9 ± 0.2
TNF-α (HEK 293) Human	1.1 ± 0.1	1.2 ± 0.2	1.5 ± 0.1

3.4 Cytokine diffusion is restricted in lymph node tissue compared to agarose:

Unlike dextran, cytokines are expected to bind to the extracellular matrix and to cell-surface receptors, which should reduce the effective diffusion coefficient (9, 43). This

phenomenon is thought to enhance the local accumulation of cytokines near pockets of secreting cells, generating local “niches” and gradients of chemokines that mediate cell behavior in immunity (5, 40, 42). To isolate the effect of binding, we directly compared the diffusion of three cytokines – TNF-α, IL-2, and IFN-γ, in a slice of agarose gel vs in tissue. We selected 2 % agarose because this density best reproduced the tortuosity of lymph node tissue for a 10-kDa dextran (Fig. 3d), indicating that in the absence of binding, 2 % agarose presents a similar barrier to diffusion as the lymph node matrix. Like dextran, all cytokines exhibited slightly restricted diffusion in 2 % agarose when compared to free solution (Table 1). Additionally, unlike the 10-kDa dextran, all cytokines experienced increased hindrance in lymph node slices compared to 2 % agarose (Table 3, Figure 5). This result indicates that binding does impede the diffusion of cytokines in lymph node tissue. In future experiments, it will be informative to use receptor knockouts, binding inhibitors, and mutant non-binding cytokines to determine the extent to which specific binding interactions contribute to local accumulation of cytokines and chemokines.

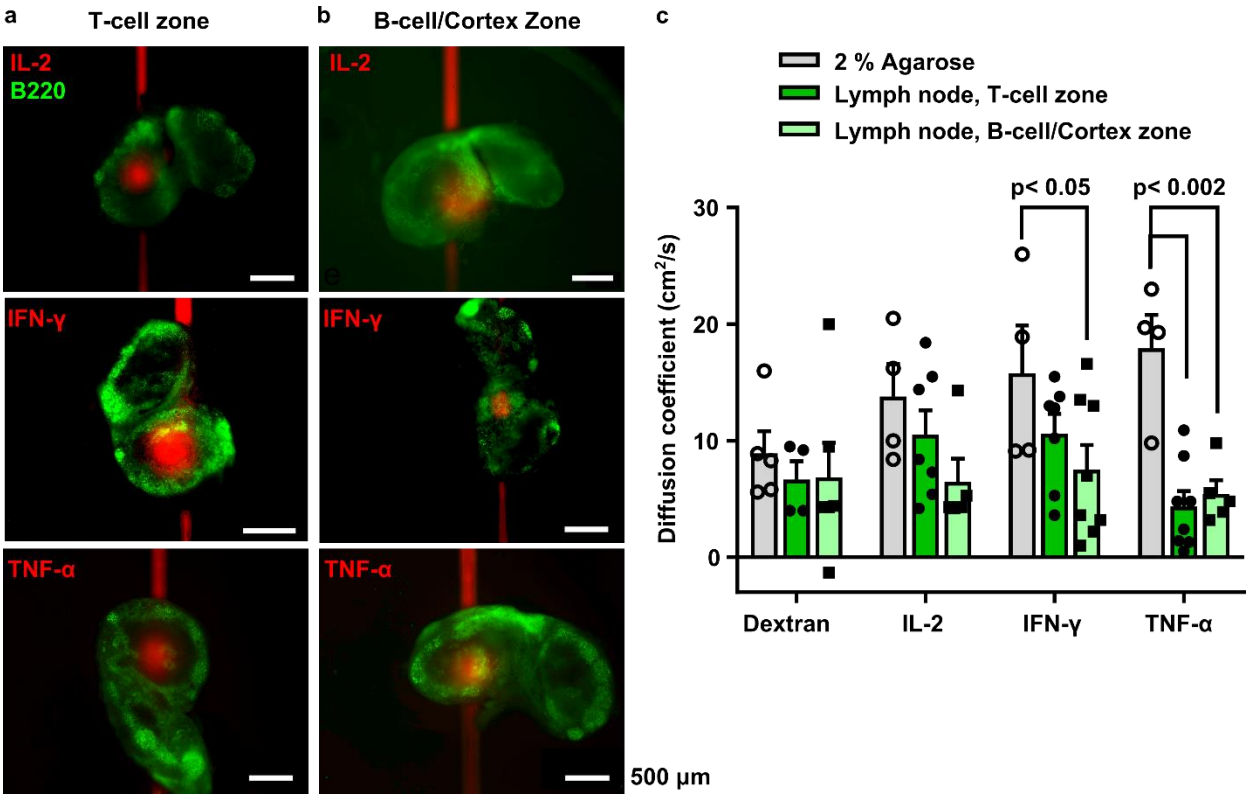

Figure 5: Diffusion of cytokines was restricted in live lymph node slices. (a, b) Representative images of Alexa Fluor 647-labelled human cytokines (red) delivered to the T-cell and the B-cell/Cortex zones of murine lymph node slices. Slices were stained in advance with FITC-anti-mouse B220 (green). (c) Unlike dextran, the cytokines trended towards increased hindrance in tissue compared to 2 % agarose. Analyzed by 2-way ANOVA with Dunnett's multiple comparison test.

We further tested the extent to which diffusion coefficients of cytokines varied between regions of the lymph node. Microfluidic delivery was able to deliver selectively to the T cell zone, while deliveries to B cell follicles sometimes spread into the surrounding cortex. On average, most cytokines trended towards more restricted diffusion in the B-cell/Cortex zone compared to the T-cell zone (Fig. 5), with the exception of mouse TNF-α, where the diffusion in the T cell zone was just as restricted as the B cell zone. Despite the trend observed between the two zones, there was large variability between individual tissue samples (SI Fig. 6 and 7), and none of the diffusion coefficients were significantly different in one zone vs another (2-way ANOVA, $p>0.05$). In addition, a limitation of the method was that for smaller B cell follicles, the linescan along which diffusion was analyzed sometimes extended beyond the follicle into the T cell zone. Future work with higher-resolution delivery may permit better distinction between the various zones.

3.5 Diffusion of glycosylated versus non-glycosylated cytokines in lymph node tissue:

Glycosylation affects protein structure and oligomerization, facilitates binding to receptors and the extracellular matrix, and regulates multiple immune pathways (63, 64). Most commercially available recombinant murine cytokines, including the ones used in this study, are expressed in E. coli and are therefore unglycosylated. We hypothesized that glycosylated cytokines would experience an increase in restricted diffusion when compared to non-glycosylated cytokines because of enhanced binding to the extracellular matrix, and, for TNF-α, enhanced oligomerization from monomer to trimer. Because the murine cytokines were not available in a mammalian expression system, we chose human cytokines expressed in mammalian cells (HEK

293) as an alternative. Fortunately, human IL-2 and TNF-α are both active in mouse tissue: Human IL-2 binds all forms of the mouse IL-2 receptor (65), and human TNF-α binds the mouse TNFR1 receptor but not the TNFR2 receptor (66, 67). Human IFN-γ is not expected to bind mouse IFN-γ receptors (68) and was therefore excluded from the study. When diffusion was measured, the human IL-2 displayed significantly hindered diffusion in tissue compared to 2% agarose, while human TNF-α trended in this direction for the B cell zone only (SI. Fig. 8)). Surprisingly, no significant differences in diffusion were observed for glycosylated vs unglycosylated cytokines, when comparing within each cytokine (Table 1; unpaired t-test, $p>0.05$). This suggested either that glycosylation (and the associated species change) did not impact diffusion to a detectable degree, or that available binding sites were saturated at the concentrations used.

We note that a large quantity of cytokine (0.01 mg mL^{-1}, 590 nM; 3.3 ng total) was delivered in this assay, to ensure visibility of the probe by fluorescence microscopy. It is possible that this high concentration saturated all available binding sites and masked any differences in binding between cytokines. To test whether effective diffusion was inflated by this effect, we tested the lowest concentration of fluorescently labelled human IL-2 that was visible (0.001 mg mL^{-1}, 59 nM). Human IL-2 was chosen because of its proper glycosylation and ability to bind IL-2 receptors in mouse tissue. The effective diffusion coefficients were unaffected by the change in concentration (SI Fig. 9), suggesting that either glycosylation did not appreciably influence binding, or that the concentration was still above the saturation point. The K_d for IL-2-receptor binding is 10 pM – 10 nM, depending on which components of its multi-unit receptor are present (69), and the K_d for cytokine binding to heparin in extracellular environment ranges from < 10 – 500 nM) (70). Future experiments will test whether the diffusion of chemokines, whose function depends on matrix binding (42), would show a larger effect of glycosylation than the cytokines tested here.

4. Conclusions:

In summary, we present a novel method to analyze diffusion of bioactive analytes in live tissue samples, and utilize this method to obtain the first direct measurements of cytokine diffusion in lymph node tissue. Micro-IOI was validated against predictions of the Stokes-Einstein equation for diffusion in free solution and against data from FRAP in an agarose hydrogel. Cytokine diffusion within specific substructures of the murine lymph node was analyzed for recombinant murine and human IL-2 and TNF-α. The diffusion of these cytokines was hindered by binding in tissue compared to 2% agarose gel, whereas diffusion of non-binding dextran was unaffected. Diffusion of cytokines was similar in the deep paracortex (T cell zone) and the B cell follicular/cortex region. Though demonstrated for lymph node, the Micro-IOI method is applicable to any soft tissue sample that can be placed on the microchip and imaged by fluorescence microscopy, including tumor and brain tissue. In the future, the use of receptor knock-outs and binding inhibitors will provide insight at the molecular level into the causes of restricted diffusion in the lymph node. We expect that this method will be useful to quantify the impact of inflammation on the diffusion of cytokines, chemokines, and immunotherapies through the lymph node, thus informing the design of cutting-edge immunotherapies.

Author contributions:

AER and RRP designed the rationale, planned experiments, and wrote the manuscript. AER performed the experiments and analyzed the data.

Acknowledgements:

The authors thank Andrew Kinman for providing the image of the lymph node slice shown in Figure 1, Benjamin Groff for his guidance in immunostaining live tissue slices, Dr. Geoff Geise

for discussion of diffusion data, and Dr. Brian Cobb for suggestions related to cytokine glycosylation. We acknowledge generous support from an Individual Biomedical Research Award from The Hartwell Foundation, an AAI Careers in Immunology Fellowship, and the Starter Grant Award from the Society of Analytical Chemists of Pittsburgh.

References:

1. Christian, J.L. 2012. Morphogen gradients in Development: from form to function. Wiley Interdiscip. Rev. Dev. Biol. 1: 3.

2. Lander, A.D. 2013. How Cells Know Where They Are. Science. 339: 923–927.

3. Jin, T., X. Xu, and D. Hereld. 2008. Chemotaxis, chemokine receptors and human disease. Cytokine. 44: 1–8.

4. Wiig, H., and M.A. Swartz. 2012. Interstitial Fluid and Lymph Formation and Transport: Physiological Regulation and Roles in Inflammation and Cancer. Physiol. Rev. 92: 1005–1060.

5. Pompano, R.R., A.H. Chiang, C.J. Kastrup, and R.F. Ismagilov. 2017. Conceptual and Experimental Tools to Understand Spatial Effects and Transport Phenomena in Nonlinear Biochemical Networks Illustrated with Patchy Switching. 86: 333–356.

6. Griffith, L.G., and M.A. Swartz. 2006. Capturing complex 3D tissue physiology in vitro. Nat. Rev. Mol. Cell Biol. 7: 211–224.

7. Tayalia, P., and D.J. Mooney. 2009. Controlled growth factor delivery for tissue engineering. Adv. Mater. Deerfield Beach Fla. 21: 3269–3285.

8. Nicholson, C., and E. Syková. 1998. Extracellular space structure revealed by diffusion analysis. Trends Neurosci. 21: 207–215.

9. Thomas, S.N., and A. Schudel. 2015. Overcoming transport barriers for interstitial-, lymphatic-, and lymph node-targeted drug delivery. Curr. Opin. Chem. Eng. 7: 65–74.

10. Syková, E., and C. Nicholson. 2008. Diffusion in Brain Extracellular Space. Physiol. Rev. 88: 1277–1340.

11. Chen, K.C., and C. Nicholson. 2000. Changes in brain cell shape create residual extracellular space volume and explain tortuosity behavior during osmotic challenge. Proc. Natl. Acad. Sci. 97: 8306–8311.

12. Kume-Kick, J., T. Mazel, I. Vořišek, S. Hrabětová, L. Tao, and C. Nicholson. 2002. Independence of extracellular tortuosity and volume fraction during osmotic challenge in rat neocortex. J. Physiol. 542: 515–527.

13. Kouchkovsky, I. de, E. Fieremans, L. Fleysher, J. Herbert, R.I. Grossman, and M. Inglese. 2016. Quantification of normal-appearing white matter tract integrity in multiple sclerosis: a diffusion kurtosis imaging study. J. Neurol. 263: 1146.

14. Wolak, D.J., and R.G. Thorne. 2013. Diffusion of Macromolecules in the Brain: Implications for Drug Delivery. Mol. Pharm. 10: 1492–1504.

15. Alexander, A.L., J.E. Lee, M. Lazar, and A.S. Field. 2007. Diffusion Tensor Imaging of the Brain. Neurother. J. Am. Soc. Exp. Neurother. 4: 316–329.

16. Rayan, G., J.-E. Guet, N. Taulier, F. Pincet, and W. Urbach. 2010. Recent Applications of Fluorescence Recovery after Photobleaching (FRAP) to Membrane Bio-Macromolecules. Sensors. 10: 5927–5948.

17. Rice, M.E., and C. Nicholson. 1989. Measurement of Nanomolar Dopamine Diffusion Using Low-Noise Perfluorinated Ionomer Coated Carbon-Fiber Microelectrodes and High-Speed Cyclic Voltammetry. Anal. Chem. 61: 1805–1810.

18. Nicholson, C., and L. Tao. 1993. Hindered diffusion of high molecular weight compounds in brain extracellular microenvironment measured with integrative optical imaging. Biophys. J. 65: 2277–2290.

19. Xiao, F., J. Hrabe, and S. Hrabetova. 2015. Anomalous Extracellular Diffusion in Rat Cerebellum. Biophys. J. 108: 2384–2395.

20. Stroh, M., W.R. Zipfel, R.M. Williams, W.W. Webb, and W.M. Saltzman. 2003. Diffusion of nerve growth factor in rat striatum as determined by multiphoton microscopy. Biophys. J. 85: 581–588.

21. Ross, A.E., M.D. Nguyen, E. Privman, and B.J. Venton. 2014. Mechanical stimulation evokes rapid increases in extracellular adenosine concentration in the prefrontal cortex. J. Neurochem. 130: 50–60.

22. Kozai, T.D.Y., A.S. Jaquins-Gerstl, A.L. Vazquez, A.C. Michael, and X.T. Cui. 2015. Brain tissue responses to neural implants impact signal sensitivity and intervention strategies. ACS Chem. Neurosci. 6: 48–67.

23. Bianchi, M.E. 2007. DAMPs, PAMPs and alarmins: all we need to know about danger. J. Leukoc. Biol. 81: 1–5.

24. Pluen, A., P.A. Netti, R.K. Jain, and D.A. Berk. 1999. Diffusion of macromolecules in agarose gels: comparison of linear and globular configurations. Biophys. J. 77: 542.

25. Johnson, E.M., D.A. Berk, R.K. Jain, and W.M. Deen. 1996. Hindered diffusion in agarose gels: test of effective medium model. Biophys. J. 70: 1017–1023.

26. Sniekers, Y.H., and C.C. van Donkelaar. 2005. Determining Diffusion Coefficients in Inhomogeneous Tissues Using Fluorescence Recovery after Photobleaching. Biophys. J. 89: 1302–1307.

27. Cornelissen, L.H., D. Bronneberg, C.W.J. Oomens, and F.P.T. Baaijens. 2008. Diffusion measurements in epidermal tissues with fluorescent recovery after photobleaching. Skin Res Technol. 14: 462–467.

28. Binder, D.K., M.C. Papadopoulos, P.M. Haggie, and A.S. Verkman. 2004. *In Vivo* Measurement of Brain Extracellular Space Diffusion by Cortical Surface Photobleaching. J. Neurosci. 24: 8049–8056.

29. Germain, R.N., M. Bajénoff, F. Castellino, M. Chieppa, J.G. Egen, A.Y.C. Huang, M. Ishii, L.Y. Koo, and H. Qi. 2008. Making friends in out-of-the-way places: how cells of the immune system get together and how they conduct their business as revealed by intravital imaging. Immunol. Rev. 221: 163–181.

30. Qi, H., W. Kastenmüller, and R.N. Germain. 2014. Spatiotemporal Basis of Innate and Adaptive Immunity in Secondary Lymphoid Tissue. Annu. Rev. Cell Dev. Biol. 30: 141–167.

31. Willard-Mack, C.L. 2006. Normal Structure, Function, and Histology of Lymph Nodes. Toxicol. Pathol. 34: 409–424.

32. Yang, C.-Y., T.K. Vogt, S. Favre, L. Scarpellino, H.-Y. Huang, F. Tacchini-Cottier, and S.A. Luther. 2014. Trapping of naive lymphocytes triggers rapid growth and remodeling of the fibroblast network in reactive murine lymph nodes. Proc. Natl. Acad. Sci. U. S. A. 111: E109-118.

33. 1990. Cytokines: Coordinators of Immune and Inflammatory Responses. Annu. Rev. Biochem. 59: 783–836.

34. Kelso, A. 1998. Cytokines: Principles and prospects. Immunol. Cell Biol. 76: 300–317.

35. Delavallée, L., E. Assier, A. Denys, G. Falgarone, J.-F. Zagury, S. Muller, N. Bessis, and M.-C. Boissier. 2008. Vaccination with cytokines in autoimmune diseases. Ann. Med. 40: 343–351.

36. Kopf, M., M.F. Bachmann, and B.J. Marsland. 2010. Averting inflammation by targeting the cytokine environment. Nat. Rev. Drug Discov. 9: 703–718.

37. Lipiäinen, T., M. Peltoniemi, S. Sarkhel, T. Yrjönen, H. Vuorela, A. Urtti, and A. Juppo. 2015. Formulation and Stability of Cytokine Therapeutics. J. Pharm. Sci. 104: 307–326.

38. Schmitz, M.L., A. Weber, T. Roxlau, M. Gaestel, and M. Kracht. 2011. Signal integration, crosstalk mechanisms and networks in the function of inflammatory cytokines. Biochim. Biophys. Acta BBA - Mol. Cell Res. 1813: 2165–2175.

39. Perona-Wright, G., K. Mohrs, and M. Mohrs. 2010. Sustained signaling by canonical helper T cell cytokines throughout the reactive lymph node. Nat. Immunol. 11: 520–526.

40. Oyler-Yaniv, A., J. Oyler-Yaniv, B.M. Whitlock, Z. Liu, R.N. Germain, M. Huse, G. Altan-Bonnet, and O. Krichevsky. 2017. A Tunable Diffusion-Consumption Mechanism of Cytokine Propagation Enables Plasticity in Cell-to-Cell Communication in the Immune System. Immunity. 46: 609–620.

41. Thurley, K., D. Gerecht, E. Friedmann, and T. Höfer. 2015. Three-Dimensional Gradients of Cytokine Signaling between T Cells. PLoS Comput. Biol. 11.

42. Proudfoot, A.E.I. 2006. The biological relevance of chemokine-proteoglycan interactions. Biochem. Soc. Trans. 34: 422–426.

43. Vaday, G.G., and O. Lider. 2000. Extracellular matrix moieties, cytokines, and enzymes: dynamic effects on immune cell behavior and inflammation. J. Leukoc. Biol. 67: 149–159.

44. Thomas, S.N., N.A. Rohner, and E.E. Edwards. 2016. Implications of Lymphatic Transport to Lymph Nodes in Immunity and Immunotherapy. Annu. Rev. Biomed. Eng. 18: 207–233.

45. Su, B., W. Zhou, K.S. Dorman, and D.E. Jones. 2009. Mathematical Modelling of Immune Response in Tissues. 10: 9–38.

46. Cappuccio, A., P. Tieri, and F. Castiglione. 2015. Multiscale modelling in immunology: a review | Briefings in Bioinformatics | Oxford Academic. 17: 408–418.

47. Wang, Y., and D.J. Irvine. 2013. Convolution of chemoattractant secretion rate, source density, and receptor desensitization direct diverse migration patterns in leukocytes. Integr. Biol. Quant. Biosci. Nano Macro. 5: 481–494.

48. Ross, A.E., M.C. Belanger, J.F. Woodroof, and R.R. Pompano. 2017. Spatially resolved microfluidic stimulation of lymphoid tissue ex vivo. Analyst. 142: 649–659.

49. Thorne, R.G., and C. Nicholson. 2006. In vivo diffusion analysis with quantum dots and dextrans predicts the width of brain extracellular space. Proc. Natl. Acad. Sci. 103: 5567–5572.

50. Erickson, H.P. 2009. Size and Shape of Protein Molecules at the Nanometer Level Determined by Sedimentation, Gel Filtration, and Electron Microscopy. Biol. Proced. Online. 11: 32–51.

51. Mohammed, J.S., H.H. Caicedo, C.P. Fall, and D.T. Eddington. 2008. Microfluidic add-on for standard electrophysiology chambers. Lab. Chip. 8: 1048–1055.

52. Chang, T.C., A.M. Mikheev, W. Huynh, R.J. Monnat, R.C. Rostomily, and A. Folch. 2014. Parallel microfluidic chemosensitivity testing on individual slice cultures. Lab Chip. 14: 4540–4551.

53. Scott, A., K. Weir, C. Easton, W. Huynh, W.J. Moody, and A. Folch. 2013. A microfluidic microelectrode array for simultaneous electrophysiology, chemical stimulation, and imaging of brain slices. Lab. Chip. 13: 527–535.

54. Lebrun, L., and G.-A. Junter. 1993. Diffusion of sucrose and dextran through agar gel membranes. Enzyme Microb. Technol. 15: 1057–1062.

55. Tao, L., and C. Nicholson. 1996. Diffusion of albumins in rat cortical slices and relevance to volume transmission. Neuroscience. 75: 839–847.

56. Pomfret, R., G. Miranpuri, and K. Sillay. 2013. The Substitute Brain and the Potential of the Gel Model. Ann. Neurosci. 20: 118.

57. Liang, S., J. Xu, L. Weng, H. Dai, X. Zhang, and L. Zhang. 2006. Protein diffusion in agarose hydrogel in situ measured by improved refractive index method. J. Controlled Release. 115: 189–196.

58. Kaldjian, E.P., J.E. Gretz, A.O. Anderson, Y. Shi, and S. Shaw. 2001. Spatial and molecular organization of lymph node T cell cortex: a labyrinthine cavity bounded by an epithelium-like monolayer of fibroblastic reticular cells anchored to basement membrane-like extracellular matrix. Int. Immunol. 13: 1243–1253.

59. Katakai, T., T. Hara, M. Sugai, H. Gonda, and A. Shimizu. 2004. Lymph Node Fibroblastic Reticular Cells Construct the Stromal Reticulum via Contact with Lymphocytes. J. Exp. Med. 200: 783–795.

60. Mueller, S.N., and R.N. Germain. 2009. Stromal cell contributions to the homeostasis and functionality of the immune system. Nat. Rev. Immunol. 9: 618–629.

61. Zanetti-Domingues, L.C., C.J. Tynan, D.J. Rolfe, D.T. Clarke, and M. Martin-Fernandez. 2013. Hydrophobic Fluorescent Probes Introduce Artifacts into Single Molecule Tracking Experiments Due to Non-Specific Binding. PLOS ONE. 8: e74200.

62. Pluen, A., Y. Boucher, S. Ramanujan, T.D. McKee, T. Gohongi, E. di Tomaso, E.B. Brown, Y. Izumi, R.B. Campbell, D.A. Berk, and R.K. Jain. 2001. Role of tumor-host interactions in interstitial diffusion of macromolecules: cranial vs. subcutaneous tumors. Proc. Natl. Acad. Sci. U. S. A. 98: 4628–4633.

63. Chamorey, A.-L., N. Magné, X. Pivot, and G. Milano. 2002. Impact of glycosylation on the effect of cytokines. A special focus on oncology. Eur. Cytokine Netw. 13: 154–160.

64. Johnson, J.L., M.B. Jones, S.O. Ryan, and B.A. Cobb. 2013. The regulatory power of glycans and their binding partners in immunity. Trends Immunol. 34: 290–298.

65. Liu, K.D., W.C. Greene, and M.A. Goldsmith. 1996. The α chain of the IL-2 receptor determines the species specificity of high-affinity IL-2 binding. Cytokine. 8: 613–621.

66. Lewis, M., L.A. Tartaglia, A. Lee, G.L. Bennett, G.C. Rice, G.H. Wong, E.Y. Chen, and D.V. Goeddel. 1991. Cloning and expression of cDNAs for two distinct murine tumor necrosis factor receptors demonstrate one receptor is species specific. Proc. Natl. Acad. Sci. U. S. A. 88: 2830–2834.

67. MacEwan, D.J. 2002. TNF ligands and receptors – a matter of life and death. Br. J. Pharmacol. 135: 855–875.

68. Hemmi, S., G. Merlin, and M. Aguet. 1992. Functional characterization of a hybrid human-mouse interferon gamma receptor: evidence for species-specific interaction of the extracellular receptor domain with a putative signal transducer. Proc. Natl. Acad. Sci. U. S. A. 89: 2737–2741.

69. Smith, K.A. 2006. The structure of IL2 bound to the three chains of the IL2 receptor and how signaling occurs. Med. Immunol. 5: 3.

70. Peysselon, F., and S. Ricard-Blum. 2014. Heparin-protein interactions: from affinity and kinetics to biological roles. Application to an interaction network regulating angiogenesis. Matrix Biol. J. Int. Soc. Matrix Biol. 35: 73–81.